CrossMark

Characteristics of surface and electrochemical properties of composites with fumed metal oxides and hydroxyapatite

E. Skwarek[1] · W. Janusz[1] · V. M. Gun'ko[2] · E. M. Pakhlov[2] · V. I. Zarko[2] · K. Gdula[1]

Abstract Hydroxyapatite composite is a very important biomaterial, which can be applied in various life areas. Hydroxyapatite and its composites with fumed oxides ST20, AST1, Al_2O_3, A90, and A300 were prepared and studied using X-ray diffraction, Fourier transform infrared spectroscopy (FTIR), scanning electron microscopy adsorption, potentiometric titration, quasi-elastic light scattering and zeta potential measurements. The values of pH_{pzc} (the point of zero charge) and pH_{IEP} (the isoelectric point) characteristic of the electrical double layer depend on the type of the fumed oxide matrix. Comparative studies of hydroxyapatite, fumed oxides and composites by adsorption and desorption of nitrogen, scanning electron microscopy and FTIR showed that in most cases composites have properties intermediate between hydroxyapatite and the oxides taken for the synthesis.

Keywords Surface · Hydroxyapatite · Fumed oxides · Composites · pH_{pzc} i pH_{IEP}

1 Introduction

In recent years, intense research has been carried out to obtain biocompatible hydroxyapatite composites with desired biological, physical and mechanical properties. Hydroxyapatite and its composites are interesting materials with a wide range of applications in medicine. Physical and chemical properties and biocompatibility with human tissues make them a very attractive object of in vivo and in vitro researches (Janusz et al. 2008; Skwarek et al. 2014).

Synthesis of porous materials with a large specific surface area and a large pore volume is essential from the point of view of their improvement to be applied in already used processes and new technologies (Holst and Cooper 2010). Synthetic hydroxyapatite can be very useful for restoration of teeth and bones because of crystallographic and chemical similarity of them. Its adsorption properties are also of significant importance (Hench 1991). Hydroxyapatite has been studied and widely clinically applied as bioactive coating of implants (Narasaraju and Phebe 1996). Hydroxyapatite coating of implants provides not only bioactivity but also a protective layer against metal ions release. As a result, an exterior coating of hydroxyapatite covering it combined with a titania layer is indispensable for preservation of hydroxyapatite bioactivity and completely protects the bounded layer with the dynamic body environment even when TiO_2 can be corroded (Chen et al. 2006). Unfortunately, poor mechanical properties of these bioceramics are one of the most serious obstacles for their wider application Therefore much effort was made to improve mechanical properties of hydroxyapatite. Mechanical properties of ceramics could be improved introducing very strengthening means. Biocompatibility is one of the important factors as for strengthening means (Hench and Wilson 1993). Investigations on various strengthening agents have been carried out in order to improve mechanical properties of hydroxyapatite. Alumina and other metal oxides can be used for these purposes. When alumina plates are added, resistance to brittle cracking grows. However, improvement of strength is

✉ E. Skwarek
ewunias@hektor.umcs.lublin.pl

[1] Faculty of Chemistry, Maria Curie-Sklodowska University, Maria Curie-Sklodowska Sq. 5, 20-031 Lublin, Poland

[2] Chuiko Institute of Surface Chemistry, Kiev 17 Naumov Str., Kiev 03164, Ukraine

minimal due to formation of microcracks around the plates because of a great difference in the coefficients of thermal expansion of Al_2O_3 and hydroxyapatite. On the other hand, when alumina powder was used as strengthening, the strength increased with increasing amount of Al_2O_3. However, further improvement of mechanical properties is difficult because of incompleteness of the mixture and excessive reactions between alumina and hydroxyapatite. In order to improve the mechanical properties of the composite, the mixing process should be improved and the reaction between alumina and hydroxyapatite should be prevented (Champion et al. 1996). Hydroxyapatite is promising for environment protection as deposited on TiO_2 capable of decomposition of volatile organic compounds (VOC), such as trichloroethylene and tetrochloroethylene at 450–500 °C. Moreover, hydroxyapatite is capable for adsorption but not decomposition of these adsorbates (Nishikawa and Monma 1994). Surface OH groups on hydroxyapatite are active sites to adsorb CO_2, CO, NO_x, H_2O and organic compounds (Hu et al. 2007). It was found that increase in NO_x oxidation mainly proceeds owing to adsorption on a surface of hydroxyapatite created on a filter. Another very interesting application of composites of mixed oxides and hydroxyapatite such as Al_2O_3/TiO_2/hydroxyapatite was elaborated for air purification. The filters proved to absorb effectively and decompose organic substances suspended in air (Nonami et al. 2004). The filter Al_2O_3/TiO_2/hydroxyapatite can be applied for CO gas removal by absorption.

In the present study, hydroxyapatite was precipitated on samples of fumed individual (silica, alumina) and complex (silica/titania and alumina/silica/titania) oxides. Surface and electrochemical properties of the composites were studied using a set of methods. The novelty of the study comes from by the kind of metal oxides prepared by the pyrogenic method used for formation of composites and studies of structure of double layer created at the composite/electrolyte solution interface.

2 Experimental

2.1 Preparation of hydroxyapatite (HAP)

Calcium acetate ($(CH_3COO)_2Ca$, Fluka) and dipotassium hydrophosphate K_2HPO_4 (POCh, Gliwice) were used upon HAP synthesis. The solutions at concentrations of 0.1 mol/dm^3 K_2HPO_4 and 0.06 mol/dm^3 $(CH_3COO)_2Ca$ were prepared. In the reaction, there was taken 0.15 dm^3 of each salt and both solutions were dropped into 0.2 dm^3 of water placed in a reaction flask. The flask was immersed in a water bath heated up to 100 °C. The salt solutions were dropped in for 30 min and then the reaction mixture was

boiled for 1 h. The mixture was stirred vigorously and the constant temperature. The obtained sediment was washed with bidistilled water to obtain a constant value of electrical conductivity of the used liquid (Suzuki et al. 1998).

The synthesis of hydroxyapatite was conducted on several oxide matrices using the described method. Such five fumed oxides as ST20 (20 % TiO_2; 80 % SiO_2); A300 (100 % SiO_2); A90 (100 % SiO_2); alumina (100 % Al_2O_3); AST1 (89 % Al_2O_3; 10 % SiO_2; 1 % TiO_2) (pilot plant of the Chuiko Institute of Surface Chemistry, Kalush, Ukraine) were used (these fumed oxides were described in detail elsewhere (Gun'ko et al. 2007, 2009). The prepared composites were washed many times to clean them from impurities.

2.2 Surface characterization

Studies of X-ray diffraction (XRD) radiation diffraction were carried out using a diffractometer Empyrean PANalytical (lamp CULEF HR, detector-pixel-3D, active canals 255). The minimal size of the step of glancing angle and scattering angle was 0.0001°.

2.2.1 Studies of FTIR were carried FTIR Nicolet 8700A (Thermo Scientific)

The textural characteristics were determined using low-temperature (77.4 K) nitrogen adsorption–desorption using a Micromeritics ASAP 2420 (V2.09) adsorption analyzer. The specific surface area (S_{BET}) was calculated according to the standard BET method (Gregg and Sing 1982). The total pore volume V_p was evaluated from the nitrogen adsorption at $p/p_0 \approx 0.99$, where p and p_0 denote the equilibrium and saturation pressure of nitrogen at 77.4 K, respectively. The nitrogen desorption data were used to compute the pore size distributions (PSDs, differential $f_V(R) \sim dV_p/dR$ and $f_S(R) \sim dS/dR$) using a self-consistent regularization (SCR) procedure under non-negativity condition ($f_V(R) \geq 0$ at any pore radius R) at a fixed regularization parameter $\alpha = 0.01$ with a complex pore model with slit-shaped (S) and cylindrical (C) pores and voids (V) between spherical nonporous nanoparticles packed in random aggregates (SCV/SCR model) (Gun'ko 2014). The differential PSDs with respect to pore volume $f_V(R) \sim dV/dR$, $\int f_V(R)dR \sim V_p$ were re-calculated to incremental PSD (IPSD) at $\Phi_V(R_i) = (f_V(R_{i+1}) + f_V(R_i))(R_{i+1} - R_i)/2$ at $\sum \Phi_V(R_i) = V_p$. The $f_V(R)$ and $f_S(R)$ functions were also used to calculate contributions of micropores (V_{micro} and S_{micro} at 0.35 nm $< R <$ 1 nm), mesopores (V_{meso} and S_{meso} at 1 nm $< R <$ 25 nm), and macropores (V_{macro} and S_{macro} at 25 nm $< R <$ 100 nm).

High resolution scanning electro-ionic microscope Quanta 3D FEG (FEI) was used to characterize the sample morphology.

Grain sizes were measured using a Mastersizer 2000 device (Malvern Instruments).

2.3 Electrochemical properties

Potentiometric titration was carried out using NaCl solutions with 0.1, 0.01, 0.001 mol/dm^3 for oxides and 0.001 mol/dm^3 for HAP and composites. Potentiometric titration measurements were performed simultaneously for suspensions of the same solid content to keep the identical conditions of the experiments in a thermostated Teflon vessel at 25 °C. To avoid the influence of CO_2, all potentiometric measurements were performed under the nitrogen atmosphere. pH values were measured using a set of glass REF 451 and calomel pHG201-8 electrodes with the Radiometer assembly. The surface charge density was calculated from the difference of the amounts of added acid or base to obtain the same pH value of suspension as for the background electrolyte.

The zeta-potential was measured using a Zetasizer 3000 (Malvern Instruments) apparatus using solutions at 0.1, 0.01, and 0.001 mol/dm^3 of NaCl. pH was measured using a PHM Beckman with combined electrodes. The dispersions were sonicated using a Sonicator XL2020 (Misonix) using 0.02 g of a sample added to a NaCl solution of a proper concentration. The pH range of 4–10 was established by addition of 0.1 mol/dm^3 of HCl or NaOH.

3 Results and discussion

3.1 Structural and textural characterization

Crystalline structure was analyzed using XRD method recording patterns at $2\theta = 10$–$80°$. Comparison of obtained patterns with the ASTM database shows that hydroxyapatites are crystalline in individual HAP and composites A90/HAP, Al_2O_3/HAP, AST1/HAP, as well as Al_2O_3 in AST1 and individual alumina. Silica in all compositions is amorphous, as well as composites ST20/HAP and A300/HAP. The presence of hydroxyapatite with low crystallinity or amorphous can be favorable for some applications of the biomaterials.

The Fourier transform infrared spectroscopy (FTIR) spectra show (Fig. 1) that particles of some composites are larger than those in individual materials since the narrower the band at 1200–900 cm^{-1}, the lager is the particles (crystallites) due to an increase in the polymerization degree (Kiselev and Lygin 1975).This is well seen for A90/HAP (Fig. 1a), Al_2O_3/HAP (Fig. 1c), and AST1/HAP (Fig. 1d), which include crystalline phases. In the case of amorphous A300/HAP, this effect is practically absent. Additionally, there is the difference in the specific surface

area of these samples because, A300/HAP is characterized by a maximal value of S_{BET} (Table 1), i.e., by a minimal size of particles.

All samples with initial fumed oxides, HAP, and composites are characterized by broad pore size distributions (PSD) (Fig. 2) because they represents nanoparticulate materials in which nanoparticles (amorphous or crystalline) form random aggregates and agglomerates of aggregates characterized by textural porosity as a set of voids between primary particles in secondary structures (Gun'ko and Turov 2013). Mesopores at pore radius of 1 nm $< R <$ 25 nm give the main contributions in both the specific surface area (Table 1, S_{meso} and S_{BET}, Fig. 2) and pore volume (V_{meso} and V_p). Such morphology of the composites is well appropriate to use them to fill polymers to prepare biomaterials (for bioengineering). As a whole, the specific surface area of composites is larger than that of individual HAP, but it is smaller than that of the initial matrices with fumed oxides. The value of S_{BET} (i.e. the average size of primary particles) of composites depends on the value of initial fumed oxides used as the matrix. Thus, selection of an appropriate matrix can allow us to change the morphology and textural characteristics of composites with HAP. A decrease in the specific surface area of composites compared to the initial fumed oxides can lead to suppression of the reaction between them and hydroxyapatite, which is considered to be a positive effect on composite strength (Kim et al. 2002).

Table 2 presents the analysis of the amounts of elements on the surface for pure hydroxyapatite. The Ca/P ratio in the powder was 1.7 which indicates slight stoichiometric excess of P in relation to hydroxyapatite (Ca/P = 1.67). Comparing hydroxyapatite and A90/HAP there can be found drop in the amounts of Ca, P and the increase of O and Si which may be the evidence that the surface A90 (SiO_2) is not fully covered with hydroxyapatite due to the synthesis.

Table 3 and Figs. 3, 4, 5, 6, 7 presents the values of grain diameters of the materials studied. The obtained results indicate that there are mainly agglomerates that is confirmed by scanning electron microscopy (SEM) images and above analysis of the morphology. As follows from the values of d (0.5) describing the average value of measured particles, the obtained composites are characterized by smaller grain size than their components, except for Al_2O_3/HAP and AST1/HAP. It is specific that alumina is in both these adsorbents. The composite AST1/HAP has the largest overage particle sizes but ST20/HAP the smallest. These data indicate that during hydroxyapatite deposition on A90, A300 and ST20, there proceeds dispersion of oxide aggregates, but for alumina and AST1, additional aggregation is observed.

Figures 8, 9, 10, 11, and 12 present the pictures from the scanning microscope for (HAP, A90/HAP, (HAP, A90/HAP, A90) Fig. 8; (HAP, A300/HAP, A300) Fig. 9; (HAP,
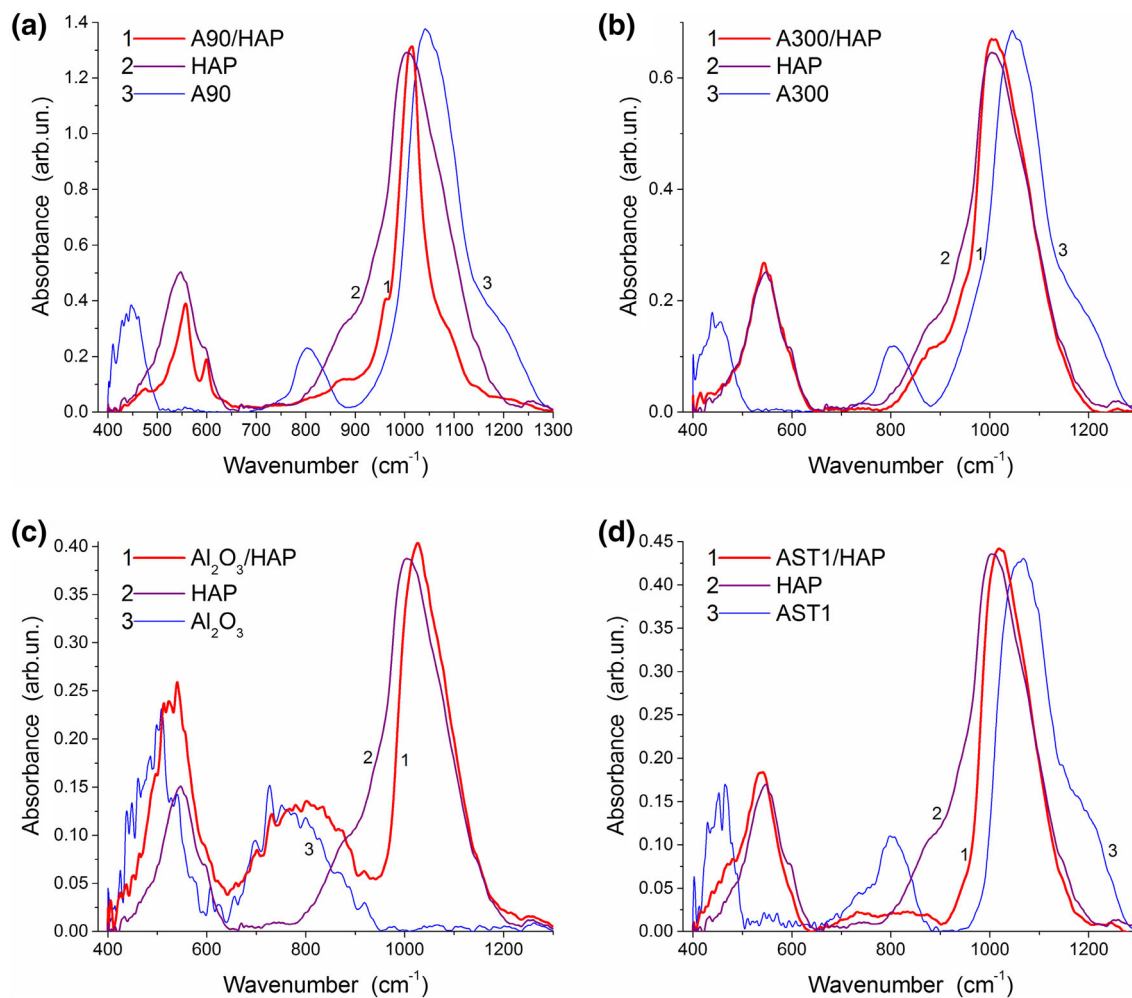
Fig. 1 FTIR spectra of **a** A90/HAP, HAP, and A90; **b** A300/HAP, HAP, and A300; **c** Al$_2$O$_3$/HAP, HAP, and Al$_2$O$_3$; and **d** AST1/HAP, HAP, and AST1

Table 1 Textural characteristics of samples

Sample	S_{BET} (m^2/g)	V_p (cm^3/g)	R (nm)	S_{micro} (m^2/g)	S_{meso} (m^2/g)	S_{macro} (m^2/g)	V_{micro} (cm^3/g)	V_{meso} (cm^3/g)	V_{macro} (cm^3/g)
HAP	29	0.14	16.88	2	24	3	0.001	0.070	0.073
ST20/HAP	51	0.22	16.26	6	40	5	0.003	0.119	0.103
ST20	81	0.22	9.89	16	62	3	0.008	0.147	0.062
A90/HAP	41	0.19	15.78	5	32	4	0.003	0.102	0.081
A90	90	0.25	9.39	16	70	4	0.009	0.157	0.082
A300/HAP	128	0.49	14.98	4	120	4	0.003	0.409	0.084
A300	297	0.80	10.18	53	232	12	0.028	0.561	0.209
Al$_2$O$_3$/ HAP	42	0.26	22.92	5	29	9	0.003	0.093	0.162
Al$_2$O$_3$	74	0.19	8.10	15	56	3	0.008	0.128	0.050
AST1/HAP	44	0.26	22.01	4	31	9	0.002	0.085	0.173
AST1	86	0.24	10.09	13	70	3	0.007	0.177	0.058

S_{BET} specific surface area, V_p total pore volume, R average pores radius from BET method
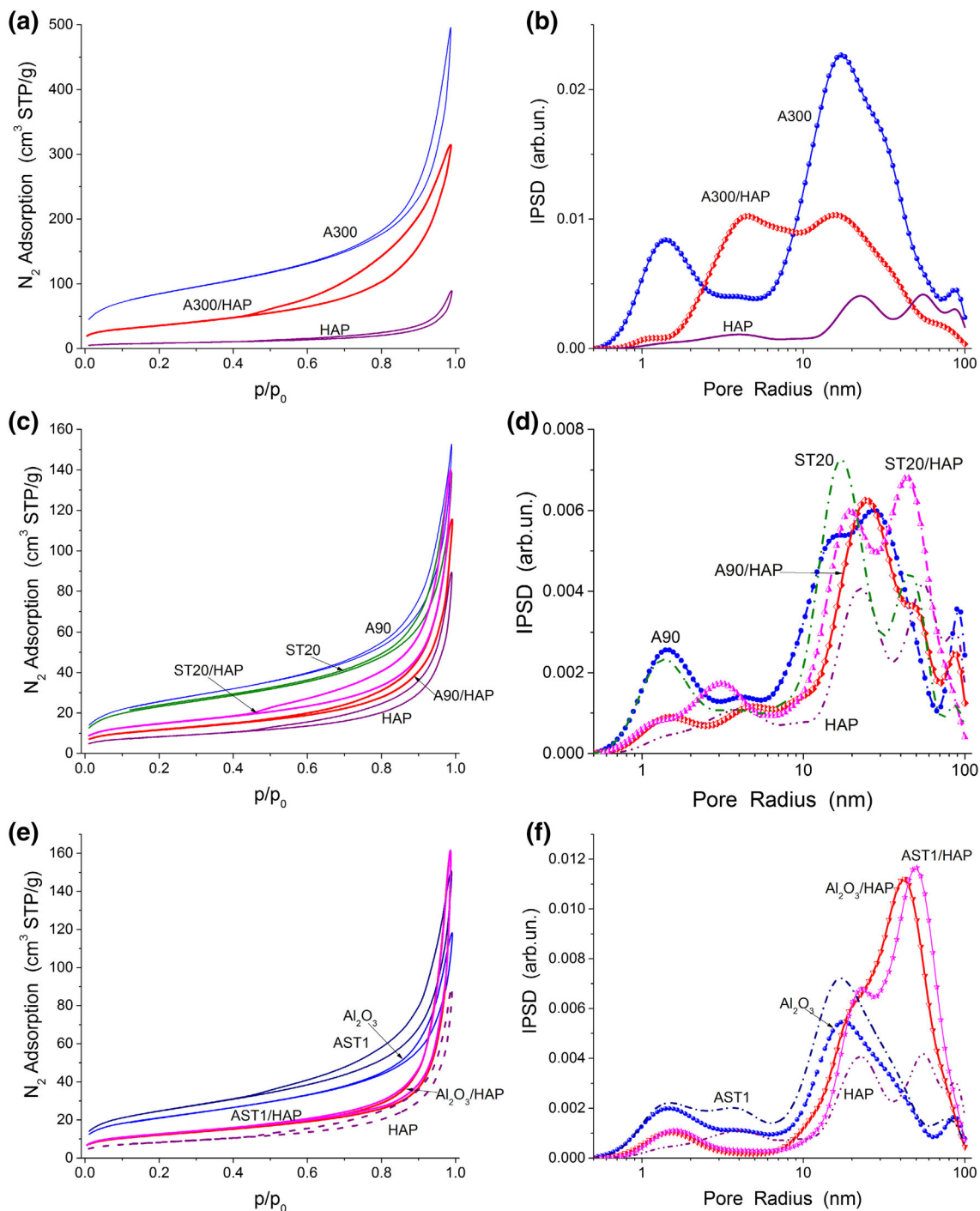
Fig. 2 **a**, **c**, **e** Nitrogen adsorption–desorption isotherms and **b**, **d**, **f** pore size distributions (SCV/SCR) for **a**, **b** A300/HAP, A300, and HAP; **c**, **d** A90/HAP, A90, ST20/HAP, ST20, and HAP; and **e**, **f** Al$_2$O$_3$/HAP, Al$_2$O$_3$, AST1/HAP, AST1, and HAP

Table 2 Contents of individual elements on the hydroxyapatite surface

	HAP		A90/HAP		A300/HAP		Al$_2$O$_3$/HAP		AST1/HAP		ST20/HAP	
	wt%	at.%	wt%	at.%	wt%	at.%	wt%	at.%	wt%	at.%	wt%	at.%
O	27	39.85	37.63	49.43	36.18	49.64	29.82	38.89	32.91	45.91	37.94	48.04
P	23.72	17.39	17.52	11.88	20.94	14.84	14.79	14.79	17.94	12.92	14.91	9.75
Ca	40.33	23.77	29.02	15.21	32.78	17.95	21.00	10.93	26	14.47	21.68	10.96

Table 3 Values of diameters characterizing adsorbent agglomerate distribution

	HAP	ST20/HAP	ST20
d (0.5) μm	5.95	4.13	8.50
	HAP	A300/HAP	A300
d (0.5) μm	5.95	5.58	16.28
	HAP	A90/HAP	A90
d (0.5) μm	5.95	5.07	2.27
	HAP	Al₂O₃/HAP	Al₂O₃
d (0.5) μm	5.95	12.04	7.53
	HAP	AST1/HAP	AST1
d (0.5) μm	5.95	5.93	5.58
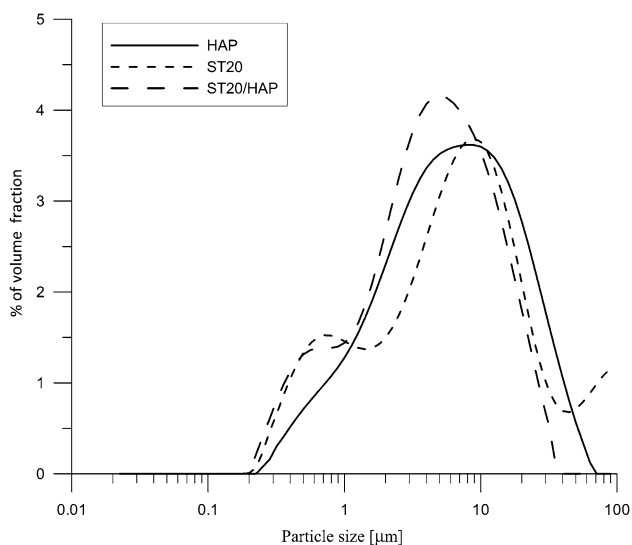
Fig. 3 Particle size analysis of hydroxyapatite sample, ST20 and ST20/HAP
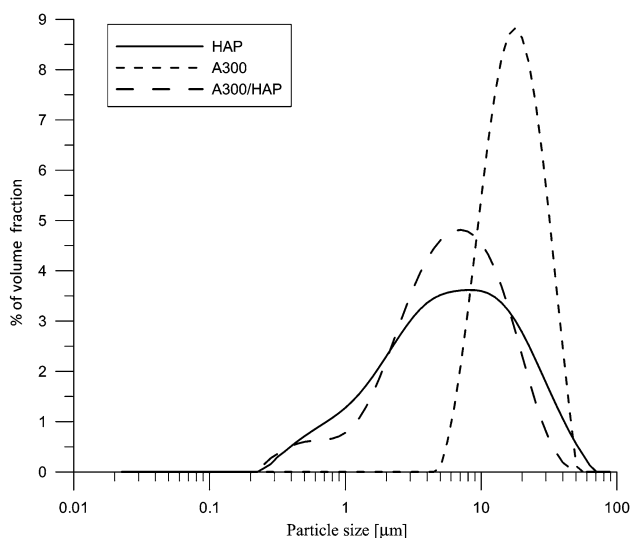
Fig. 4 Particle size analysis of hydroxyapatite sample, A300 and A300/HAP
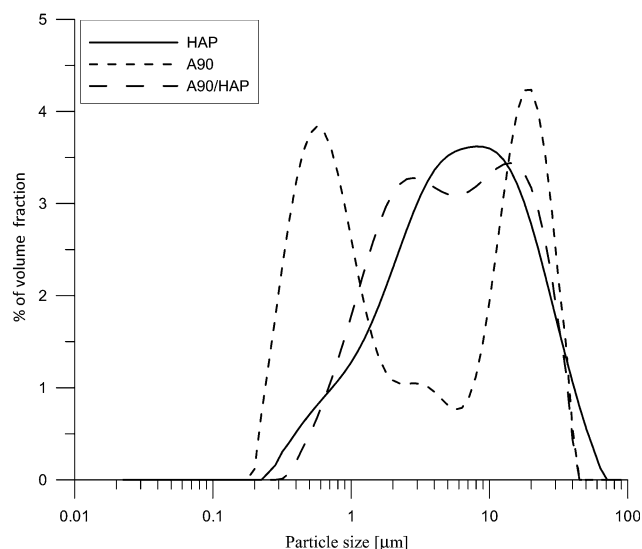
Fig. 5 Particle size analysis of hydroxyapatite sample, A90 and A90/HAP
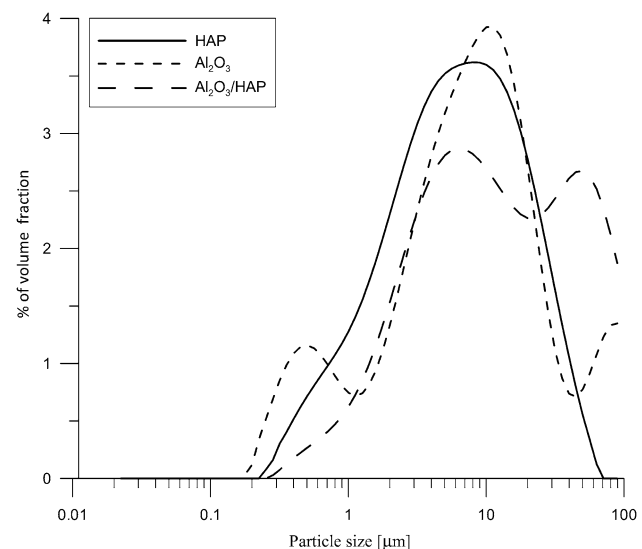
Fig. 6 Particle size analysis of hydroxyapatite sample, Al_2O_3 and Al_2O_3/HAP

Al_2O_3/HAP, Al_2O_3) Fig. 10; (HAP,AST1/HAP,AST1) Fig. 11 and (HAP,ST20/HAP,ST20) Fig. 12. Comparing the photos from the scanning microscope for pure hydroxyapatite and A90 one can see great similarity but in the case of the composite, the surface changes and is more feathery. Large aggregates can be observed.

Comparing the pictures in Fig. 9, there can be seen differences in the change of the surface of the adsorbents: A300 i A300/HAP. In the latter a characteristic form for hydroxyapatite can be observed. The results in Table 2
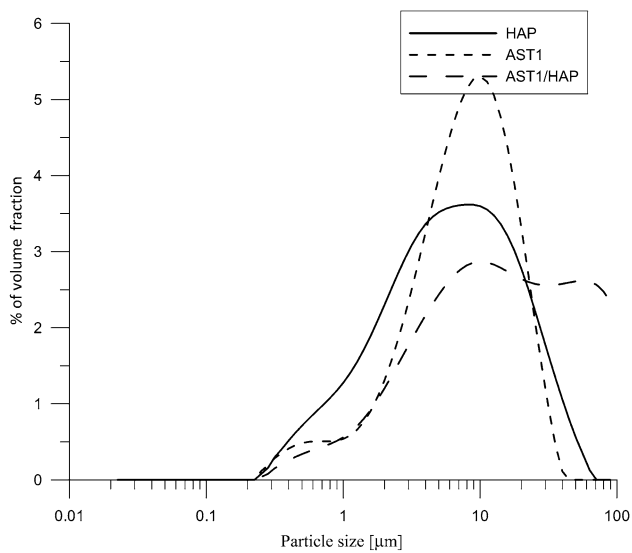
Fig. 7 Particle size analysis of hydroxyapatite sample, AST1 and AST1/HAP

confirm that on the A300/HAP surface there remained a very small amount of silica—only 0.3 % of total 32.94 %.

Figure 10 clearly shows changes of morphology of pure Al_2O_3 and Al_2O_3/HAP surfaces. In the latter one see the form very similar to that of hydroxyapatite as well single fibres, possibly Al_2O_3 between hydroxyapatite particles. The results from Table 2 show that the total percentage of aluminium on the surface was reduced by about half which can confirm large coverage of Al_2O_3 surface with hydroxyapatite deposit. Comparing the photos from the scanning microscope in Fig. 11 for samples: AST1 and AST1/HAP, one can see that crystalline forms characteristic of HAP appear for the sample AST1/HAP. The presence of this compound on the surface of Al_2O_3 confirmed by the analysis of ED-XRF.

As follows from Fig. 12 and Table 2 the composite ST20/HAP forms larger agglomerates than HAP or ST20 but on the surface there are all elements constituting these compounds. None of the elements was completely covered
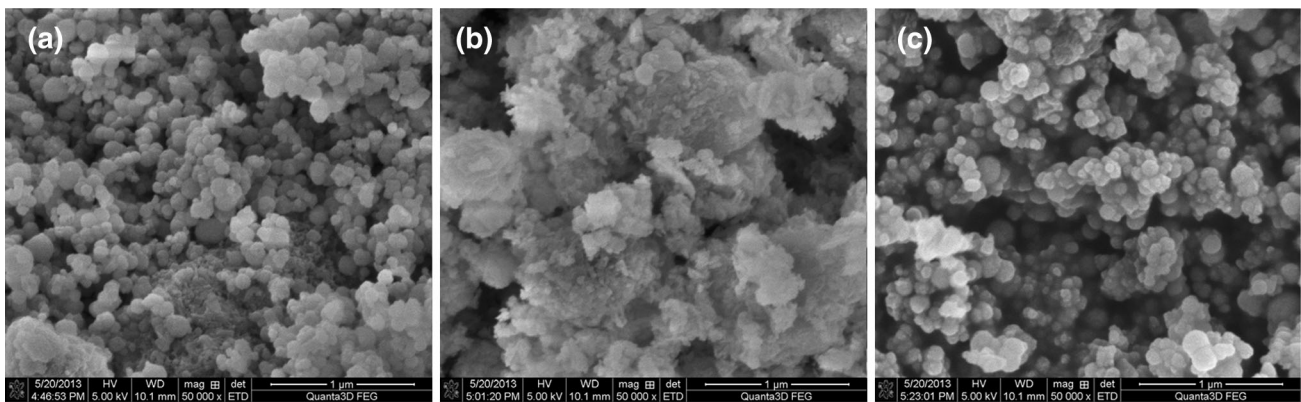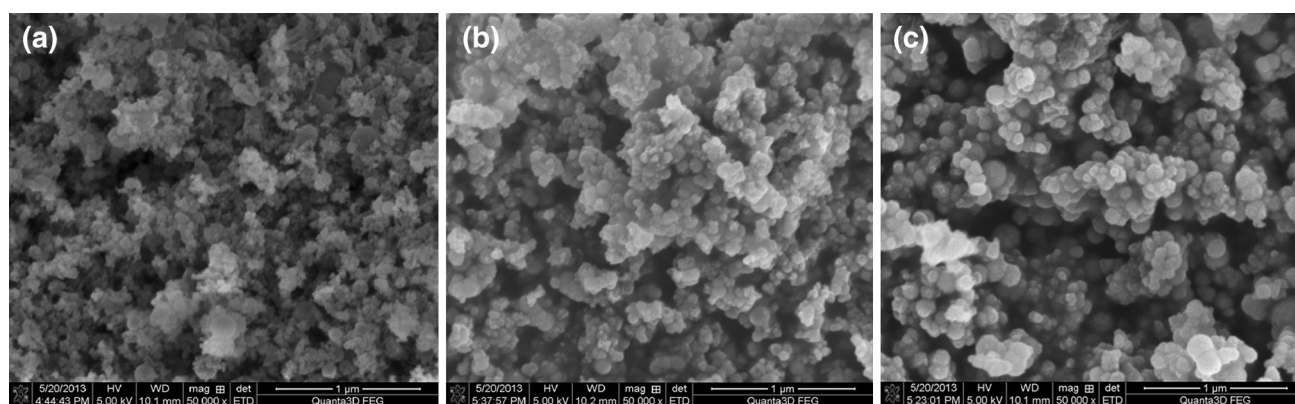

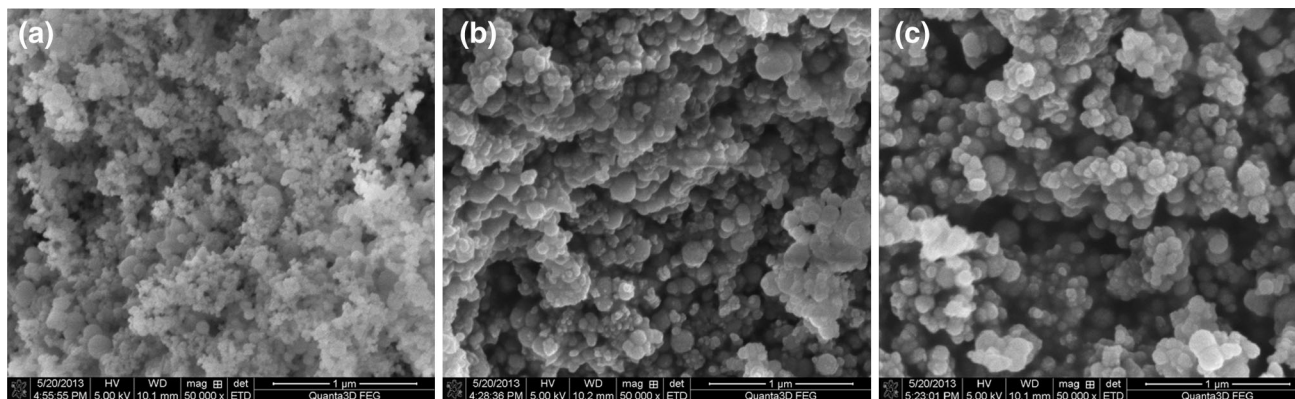Fig. 8 Picture from the scanning microscope magnified 50,000 times for: **a** A90; **b** A90/HAP; **c** HAP
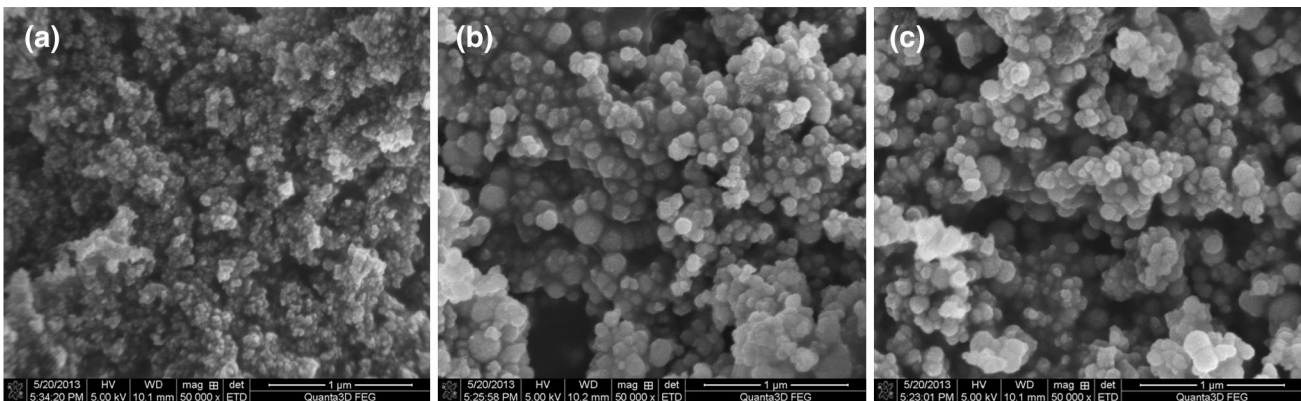
Fig. 9 Picture from the scanning microscope magnified 50,000 times for: **a** A300; **b** A300/HAP; **c** HAP
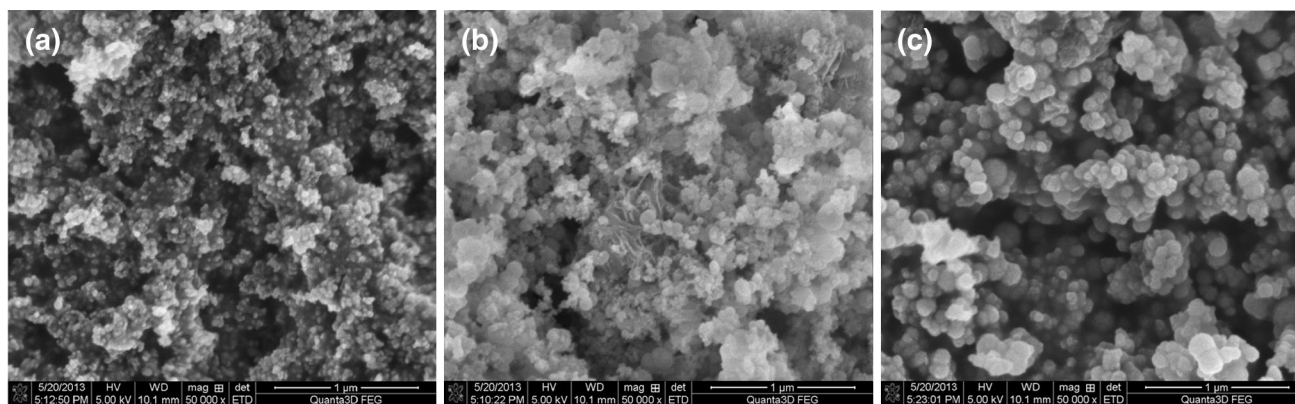
Fig. 10 Picture from the scanning microscope magnified 50,000 times for: **a** Al$_2$O$_3$; **b** Al$_2$O$_3$/HAP; **c** HAP

Fig. 11 Picture from the scanning microscope magnified 50,000 times for: **a** AST1; **b** AST1/HAP; **c** HAP

Fig. 12 Picture from the scanning microscope magnified 50,000 times for: **a** ST20; **b** ST20/HAP; **c** HAP

but they were only reduced compared to the initial substance they were components of.

3.2 Electrochemical characterization

Potentiometric titration is the most frequently applied method to determine the surface charge and position of

point of zero charge (PZC) in the metal oxide/electrolyte solutions. The important parameters characterizing the electrical double layer (EDL) are the surface charge density and PZC. The latter is the point in which the concentration of positively charged surface groups is equal to the concentration of negatively charged groups. For all samples (Table 4), higher pHpzc is for the

Table 4 Electrokinetic parameters

Adsorbents	pH$_{pzc}$	pH$_{IEP}$
HAP	8.5	<4
ST20/HAP	<7.2	<4
ST20	7.6	<4
A300/HAP	8.6	<4
A300	<3	<4
A90/HAP	6.2	<4
A90	∼3.6	<4
Al$_2$O$_3$/HAP	8.5	<4
Al$_2$O$_3$	4.5	<9.5
AST1/HAP	8.4	<4
AST1	4.5	<9.7

composites than for fumed oxides due to the effect of HAP deposits.

Zeta potential and surface charge density are important parameters characterizing EDL. The value of zeta potential can be determined based on one of four electrokinetic phenomena: sedimentation potential, flow potential, electroosmosis and microelectrophoresis. Concentration of potential creating (H^+) ions at which the zeta potential is zero is called the isoelectric point (pH$_{IEP}$). It assumes that the potential of diffusion layer is equal to the zeta potential. At pH$_{IEP}$, concentration of positively and negatively charged surface groups and ions under the slip layer are equal. As follows from Table 4, the composites have intermediate values of pH$_{IEP}$ between those for initial oxides and hydroxyapatite.

According to I.D. Smičiklas et al. (Smičiklas et al. 2000; Bell et al. 1973), pHpzc and pH$_{IEP}$ values for hydroxyapatite determined by potentiometric titration and electrophoresis in different basic electrolytes correspond to pH$_{IEP}$ < 5 for some samples. L.C. Bell and coworkers presented pHpzc from 4.35 to 7 for HAP in different electrolytes. The comparison of pHpzc and pH$_{IEP}$ position indicates that pH$_{IEP}$ is shifted by about 3 units toward the acidic side. Such shift of the points was found for the systems in which adsorption of specific ions proceeds. In the case of basic electrolyte, such situation can occur for the porous systems characterized by energetic heterogeneity of a surface. The studied samples belong to the systems characterized by the textural porosity. The pores can be "clogged" during electrophoresis measurements, and the properties of this part of solid is not disclosed. Therefore, a large part of charge can be compensated inside textural pores of aggregates and only a part coming from the ionized groups on the outer surface of secondary particles is responsible for the electrophoretic mobility.

4 Conclusions

Composites of hydroxyapatite were prepared using fumed oxides as matrices by means of the hydroxyapatite precipitation method upon the reaction of $(CH_3COO)_2Ca$ with K_2HPO_4. Studies of the crystalline structure of the composites by the XRD method showed the presence of crystalline hydroxyapatite phase. The values of pH$_{pzc}$ and pH$_{IEP}$ characteristic of the EDL depend on the type of the fumed oxide matrix. This suggests that the HAP coverage of the oxide nanoparticles are not continuous, i.e. it is clustered.

Comparative studies of HAP, fumed oxides and composites by adsorption and desorption of nitrogen, scanning electron microscopy, and FTIR showed that in most cases composites have properties intermediate between hydroxyapatite and the oxides taken for the synthesis. Measurements of the adsorption–desorption of H^+ ions by potentiometric titration has shown that the samples of tested composites, except the sample based on A90, have the affinity for the H^+ ion similar to that of hydroxyapatite.

References

Bell, L.C., Posner, A.M., Quirk, J.P.: The point of zero charge of hydroxyapatite and fluorapatite in aqueous solutions. J. Colloid Interface Sci. **42**, 250–261 (1973)

Champion, E., Gautier, S., Bernache-Assolland, D.: Characterization of hot pressed Al$_2$O$_3$-platelet reinforced hydroxyapatite composites. J. Mater. Sci. **7**, 125–131 (1996)

Chen, Y., Zhang, Y.Q., Zhang, T.H., Gan, C.H., Zheng, C.Y., Yu, G.: Carbon nanotube reinforced hydroxyapatite composite coatings produced through laser surface alloying. Carbon **44**, 37–45 (2006)

Gregg, S.J., Sing, K.S.W.: Adsorption, surface area and porosity. Academic Press, London (1982)

Gun'ko, V.M., Nychiporuk, Y.M., Zarko, V.I., Goncharuk, E.V., Mishchuk, O.A., Leboda, R., Skubiszewska-Zięba, J., Skwarek, E., Janusz, W., Yurchenko, G.R., Osovskii, V.D., Ptushinskii, Y.G., Turov, V.V., Gorbik, P.P., Blitz, J.P., Gude, K.: Relationships between surface compositions and properties of surfaces of mixed fumed oxides. Appl. Surf. Sci. **253**, 3215–3230 (2007)

Gun'ko, V.M.: Composite materials: textural characteristics. Appl. Surf. Sci. **307**, 444–454 (2014)

Gun'ko, V.M., Turov, V.V.: Nuclear Magnetic Resonance Studies of Interfacial Phenomena. CRC Press, Boca Raton (2013)

Gun'ko, V.M., Zarko, V.I., Turov, V.V., Oranska, O.I., Goncharuk, E.V., Nychiporuk, Y.M., Pakhlov, E.M., Yurchenko, G.R., Leboda, R., Skubiszewska-Zięba, J., Osovskii, V.D., Ptushinskii, Y.G., Derzhypolskyi, A.G., Melenevsky, D.A., Blitz, J.P.: Morphological and structural features of individual and composite nanooxides with alumina, silica, and titania in powders and aqueous suspensions. Powder Technol. **195**, 245–258 (2009)

Hench, L.L.: Bioceramics: from concept to clinic. J. Am. Ceram. Soc. **74**(7), 1487–1510 (1991)

Hench, L.L., Wilson, J.: An Introduction of Bioceramics, p. 139. World Scientific Publishing, Singapore (1993)

Holst, J.R., Cooper, A.I.: Ultrahigh surface area in porous solids. Adv. Mater. **22**, 5212–5216 (2010)

Hu, A., Li, M., Chang, C., Mao, D.: Preparation and characterization of a titanium-substituted hydroxyapatite photocatalyst. J. Mol. Catal. A **267**, 79–85 (2007)

Janusz, W., Skwarek, E., Złotucha, A., Reszka, M.: The study of the acid–base properties of the surface groups at the hydroxyapatite/NaClO$_4$ solution interface. Pol. J. Chem. **82**, 57–67 (2008)

Kiselev, A.V., Lygin, V.I.: Infrared Spectra of Surface Compounds. Wiley, New York (1975)

Kim, S., Kong, Y.-M., Lee, I.-S., Kin, H.-E.: Effect of calcinations of starting powder on mechanical properties of hydroxyapatite-alumina bioceramic composite. J. Mater. Sci. **13**, 307–310 (2002)

Nishikawa, H., Monma, H.: Oxidative decomposition of chlorobenzene over calcium-deficient hydroxyapatite. Bull. Chem. Soc. Jpn. **67**, 2454–2456 (1994)

Narasaraju, T.S.B., Phebe, D.E.: Some physico-chemical aspects of hydroxyapatite. J. Mater. Sci. **31**, 1–21 (1996)

Nonami, T., Hase, H., Funakoshi, K.: Syntheses, structures and photophysical properties of iron containing hydroxyapatite prepared by a modified pseudo-body solution. Catal. Today **96**, 113–118 (2004)

Skwarek, E., Janusz, W., Sternik, D.: Adsorption of citrate ions on hydroxyapatite synthetized by various methods. J. Radioanal. Nucl. Chem. **299**, 2027–2036 (2014)

Smičiklas, I.D., Milonjič, S.K., Pfendt, P., Raičević, S.: The point zero of charge and sorption of cadmium (II) and strontium(II) ions on synthetic hydroxyapatite. Sep. Purif. Technol. **18**, 185–194 (2000)

Suzuki, S., Ohgaki, M., Ichiyanagi, M., Ozawa, M.: Preparation of needle-like hydroxyapatite. J. Mater. Sci. Lett. **17**, 381–383 (1998)